Open access • Journal Article • DOI:10.1109/TWC.2010.01.090391

Modeling the ultra-wideband outdoor channel: Measurements and parameter extraction method — Source link

Telmo Santos, Johan Kåredal, Peter Almers, Fredrik Tufvesson ...+1 more authors

Institutions: Lund University, Ericsson, University of Southern California

Published on: 01 Jan 2010 - IEEE Transactions on Wireless Communications (IEEE--Institute of Electrical and Electronics Engineers Inc.)

Topics: Multipath propagation and Impulse response

Modeling the ultra-wideband outdoor channel - measurements and parameter extraction method

Santos, Telmo; Kåredal, Johan; Almers, Peter; Tufvesson, Fredrik; Molisch, Andreas

Published in:
IEEE Transactions on Wireless Communications

DOI:
10.1109/TWC.2010.01.090391

2010

Modeling the Ultra-Wideband Outdoor Channel: Measurements and Parameter Extraction Method

Telmo Santos, *Student Member, IEEE*, Johan Karedal, *Member, IEEE*, Peter Almers, Fredrik Tufvesson, *Senior Member, IEEE*, and Andreas F. Molisch, *Fellow, IEEE*

***Abstract*—This paper presents results from an outdoor measurement campaign for ultra-wideband channels at gas stations. The results are particularly relevant for "infostations" where large amounts of data are downloaded to a user within a short period of time.**

We describe the measurement setup and present a novel high-resolution algorithm that allows the identification of the scatterers that give rise to multipath components. As input, the algorithm uses measurements of the transfer function between a single-antenna transmitter and a *long* uniform linear virtual array as receiver. The size of the array ensures that the incoming waves are spherical, which improves the estimation accuracy of scatterer locations. Insight is given on how these components can be tracked in the impulse response of a spatially varying terminal.

We then group the detected scatterers into *clusters*, and investigate the angular power variations of waves arriving at the receiver from the clusters. This defines the cluster's "radiation pattern."

Using sample measurements we show how obstacles obstruct the line-of-sight component – a phenomenon commonly referred to as "shadowing." We compare the measurement data in the shadowing regions (locations of the receiver experiencing shadowing) with the theoretical results predicted by diffraction theory and find a good match between the two.

***Index Terms*—Channel parameter estimation, measurement campaign, outdoor, ultra-wideband.**

I. Introduction

OVER the past years, ultra-wideband (UWB) wireless systems have drawn considerable interest in the research community. The ultra-wide bandwidth provides high ranging accuracy, protection against multipath fading, low power spectral density and wall penetration capability [2], [3]. The applications for this innovative technology are numerous, ranging from radar systems for target identification and imaging, accurate localization and tracking as a complement to GPS [4], communications in harsh environments [5], [6] to high-data-rate connectivity [7], [8].

An intriguing application for outdoor high-data-rate connectivity are infostations [9], i.e., short-range transmitters that can operate at extremely high data rates, and thus allow a receiver to download a large amount of data within a very short period of time. A typical infostation can be placed, e.g., at a gas station, allowing wireless downloading of high-definition movies to a car within the time it takes to fill up a gas tank of a vehicle, i.e., within a few minutes. Alternative applications include road and traffic information for driving safety, and wireless payment. These, and related methods for enabling in-car entertainment, have drawn great interest from the car industry in recent years [10].

The first vital step in the design of any wireless system lies in the measurement and modeling of the relevant propagation channels. These determine the theoretical performance limits, as well as the practical performance of actual systems operating in the considered environment. To the best of our knowledge, there have been very few UWB outdoor measurement campaigns presented in the literature. References [11], [12] measured the propagation channel in rural scenarios, [13] measured in "forest," "hilly" and "sub-urban" scenarios, [12], [14] measured the propagation from an office-type environment to an outdoor device; these studies also extract purely stochastic channel models. Ray tracing (not measurements) were used to investigate channel characteristics of farm environments [15]. The results from [14], [15] also form the basis for models CM5, CM 6, and CM 9 of the IEEE 802.15.4a UWB channel model [16]. The campaign most similar to ours is the one of [17], which analyzed the channel between transceivers on a parking lot. It was found in that campaign that a geometrical model that takes the direct and ground-reflected component into account and additionally considers diffuse multipath gave a good agreement with the measured impulse responses. However, there is no measurement campaign dedicated to the infostation scenario, i.e., an outdoor environment close to a gas-station, drive-by restaurant, or similar scenario. The current paper aims to fill that gap, presenting the results of an extensive measurement campaign at two gas stations near Lund, Sweden.

Besides the presentation of sample measurement results from this campaign, the main contributions of this paper are:

- we introduce a new high-resolution algorithm for locating scatterers (interacting objects) based on the use of a large virtual antenna array combined with measurements in the

Manuscript received March 17, 2009; revised August 13, 2009; accepted October 2, 2009. The associate editor coordinating the review of this paper and approving it for publication was S. Affes.

This work was financially supported by the Swedish Strategic Research Foundation (SSF) Center of High Speed Wireless Communications (HSWC) at Lund University and by the Swedish Vetenskapsrådet.

T. Santos, J. Karedal, and F. Tufvesson are with the Department of Electrical and Information Technology, Lund University, Sweden (e-mail: {Telmo.Santos, Johan.Karedal, Fredrik.Tufvesson}@eit.lth.se).

P. Almers is with ST-Ericsson, Lund, Sweden (e-mail: Peter.Almers@stericsson.com).

A. F. Molisch is with the Department of Electrical Engineering, University of Southern California, Los Angeles, CA, USA (e-mail: Andreas.Molisch@ieee.org).

Part of this work was presented at IEEE VTC'08 Spring [1].

Digital Object Identifier 10.1109/TWC.2010.01.090391

frequency domain;
- we identify clusters of scatterers, and show that they exhibit directional properties; in other words, the power[1] of the multipath components (MPCs) associated with a cluster depends significantly on the direction of observation;
- at some locations in our scenario, the line-of-sight (LOS) between transmitter (TX) and receiver (RX) is shadowed off by an obstacle. We introduce the concept of a "shadowing region," and show that the qualitative behavior of the received signal can be explained by the simple picture of "diffraction around a plate."

Based on the measurement results presented here, the companion paper [18] derives a statistical model for infostation channels.

The remainder of this paper is organized as follows. In Section II the measurement campaign and scenarios are described. Then, Section III explains the post-processing applied to the measured data, in particular the high-resolution extraction of scatterers for each element of the virtual antenna array along with tracking, and the clustering of the detected scatterers. Subsequently, Section IV, gives insight into some characteristics of the UWB channel, in particular the nonstationary effects of cluster radiation patterns and shadowing of the LOS. Finally, Section V wraps up the paper.

II. Measurement Campaign Description

A. Measurement Equipment and Setup

Our measurements were done with a HP8720C vector network analyzer (VNA), which measures the S_{21} parameter of the device under test, namely the propagation channel. The VNA is configured to measure at $N_f = 1601$ regularly spaced frequency points in the range from 3.1 to 10.6 GHz. The intermediate frequency (IF) bandwidth was set to 1000 Hz. A UWB low noise amplifier (LNA) with a gain of 28 dB and noise figure of 3.5 dB, connected between the RX antenna and the receive port of the VNA, was used to boost the received signal-to-noise ratio (SNR), which was always above 25 dB. A "thru" calibration was performed to eliminate the effect of signal distortions by the cables and amplifier.

Measurements were performed using the virtual array principle, where channel samples at different "array elements" are obtained by mechanically moving a (single) antenna element to different positions. In our setup, the antenna emulating the mobile station (MS) antenna, was moved to various positions along an eight-meter-long plastic rail using a stepper motor. The measurement equipment was controlled by a fully configurable LabVIEW script running on a notebook computer. Both the VNA and the motor controller had general purpose interface bus (GPIB) connections to the notebook. The other antenna emulated a typical base-station (BS) or access-point (AP) in an infostation scenario, and was placed at a fixed location on top of an aluminum pole. A diagram of the measurement setup is given in Fig. 1. During measurement, the channel was static, (i.e., the only movement of any kind was the movement of the MS to different array element locations), which is a necessary condition for a virtual-array interpretation [19].

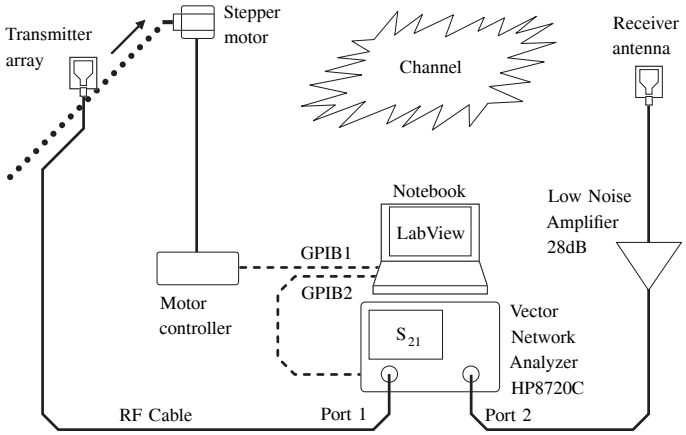

Fig. 1: UWB measurement equipment and measurement campaign setup. At every position, the notebook triggers the VNA measurement, stores the S_{21} parameter and moves the transmitter antenna.

In our campaign we measured the transfer function of the "radio propagation channel" between the antenna connectors at transmitter and receiver; the radio channel is thus defined to include both the TX and RX antennas and the actual propagation channel. Since the complete radiation pattern of the antennas was not available over the bandwidth of interest, no attempts were made to compensate the impact of the frequency-dependent antenna pattern on the measured data.

Both TX and RX antennas were stamped metal antennas from SkyCross, model SMT-3TO10M-A. They were chosen for their small size, linear phase across frequency. Preliminary measurements furthermore showed that the antenna pattern was almost omnidirectional in the azimuthal plane (with variations on the order of ± 3 dB of the time domain pulse envelope and ± 5 dB for individual frequencies), which is the dominating propagation plane in our measurement scenario. In a real infostation scenario, the mobile user antenna is expected to be on top of or inside a vehicle, leading to additional scattering, thus distorting the antenna patterns. We consciously did not include any vehicle in our campaign, for three reasons:

- by measuring with a car, the final channel model becomes specific to that type of car, and even to the particular antenna placement, used in the campaign;
- the high-resolution algorithm, and the extracted scatterer locations, require the assumption of single-scattering only; this assumption might be violated if there is significant scattering by the car on which the antenna is placed;
- the model derived from our measurements *without* the car can be combined with arbitrary car/antenna combinations through the concept of "composite channels" [20]. In this way, the final model is suitable for situations when the influence of the vehicle is well known (e.g., with a measurement setup similar to the one used in [21]) and can be introduced into the model, becoming suitable for any kind of vehicle.

[1]The term *power*, is used throughout this paper referring to the dimensionless quantity of the received to transmitted power ratio defined as $P_o/P_i = |V_o/V_i|^2$. The ratio of received to transmitted complex voltages, V_o/V_i, is the quantity measured by the vector network analyzer.

Fig. 2: Photo of one of the measurement sites. OKQ8 gas station in Södra Sandby, Sweden.

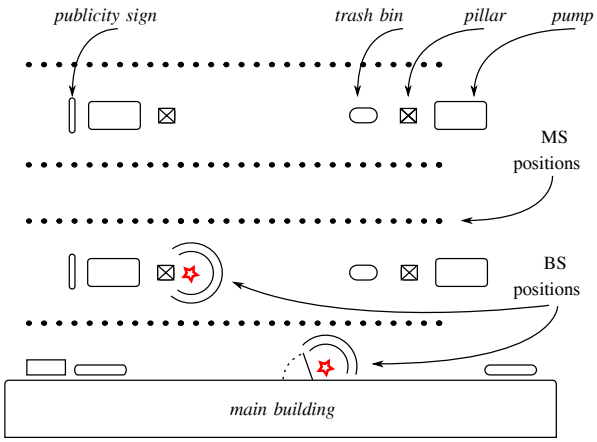

Fig. 3: Representation of the typical layout of the measured scenarios. The four dotted lines of MS positions and the two BS positions are indicated.

B. Measurement Scenarios

The measured sites were two gas stations in Sweden, Hydro in Staffanstorp and OKQ8 in Södra Sandby. A photo of the latter is given in Fig. 2. The structure of those stations is fairly similar, with a small "main building" containing a convenience store, a number of gas pumps, and a roof supported by structural columns. Comparison of the results from the two stations shows that the channel characteristics are indeed similar. This supports the conjecture that a model derived from those measurement has an applicability that goes beyond the specific measured stations.

At each location, we considered two BS positions and four straight lines (virtual arrays) of MS positions. Fig. 3 shows a representation of the measured positions. The BS was placed at a height of 2.6 m and the MS at 1.6 m. The first BS location was above the entrance to the gas station's convenience store, whereas the second location was on one of the structural pillars located on the side of one of the gas pumps. The MS positions were chosen to be where a vehicle is expected to stop or pass, namely on the sides of the gas pumps. Each MS virtual array was composed of $N_{\mathrm{MS}} = 170$ sampled positions, with spacing of 48 mm (approximately half of the largest measured wavelength, $\approx \lambda_{\max}/2$), corresponding to a total covered distance of 8.11 m. The total number of measured impulse responses is $2 \times 2 \times 4 \times 170 = 2720$. Fig. 3 also identifies the most significant scattering objects in the environment. Those objects were mostly made of metal, with the exception of the "main building" walls (which were composed of concrete and glass).

III. Post-Processing of Measurement Data

In this section we describe the post-processing applied to the measurement data. Based on the measured channel transfer functions, we try to identify the location of scatterers in the geometrical space. These extracted locations are then subsumed into clusters. The inter-cluster and intra-cluster properties provide useful insights into the physical propagation mechanisms (which are the emphasis of this paper) and also form the basis of the geometry-based stochastic channel model described in [18].

A. Scatterer Detection Method - Principles and Fundamental Assumptions

Our high-resolution scatterer detection method is similar in spirit to the CLEAN algorithm that was introduced for UWB channel sounding in [22], though it differs in some important details. Additional explanations and examples are given in [1].

It is important to note that the method relies on the previously described measurement principle, i.e. using a setup with one antenna on one of the link sides, and a virtual array of antennas on the other link side. In contrast to most existing high-resolution algorithms, which rely on the plane wave assumption, we assume (and require) the array to cover an area large enough so that *the wave fronts arriving to the array are spherical (i.e., plane wave assumption is not valid)*. Then, merging the information from all the array positions improves the detection performance. This is the key innovation of our algorithm.

Longer virtual arrays are also essential to evaluate how the MPCs evolve with changing MS positions, both in the small- and large-scale sense. Fig. 4 shows an example of all the 170 measured impulse responses from one rail. In all impulse responses, the earliest component is the strongest one, which agrees with the interpretation as the LOS. Several "lines", or specular components, can be identified from the figure indicating the presence of physical scatterers. It is also notable that some specular components cannot be observed at all MS locations, whereas others can be observed over the whole measured range of locations. The method described below, identifies these specular MPCs in the delay domain and reveals the scatterer locations in space where they originated from.

The basic principle of our algorithm for finding the specular components in the delay domain is the following: for each impulse response, we detect the strongest peak of the impulse response (using a high-resolution search) and subtract the contribution coming from the corresponding MPC from the impulse response, and then repeat the process until all significant MPCs have been detected. This can be understood as a *search and subtract* approach, which principle also underlies other popular UWB channel parameter estimation methods

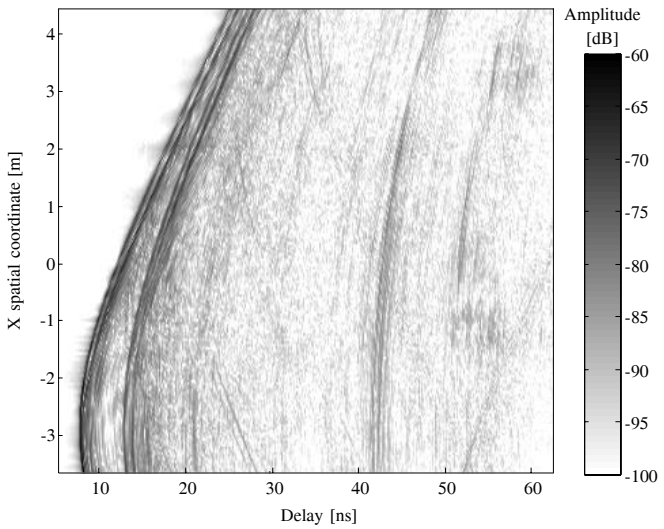

Fig. 4: Measured impulse responses along the horizontal direction covering 8.11 m.

[22], [23]. While this approach can lead to the appearance of *ghost* components (when the subtracted pulse shapes differ from the actually received ones), it can approximate the performance of maximum-likelihood detection, while being much less computationally burdensome.

It must be emphasized that our algorithm for the extraction of the scatterer location relies on several key assumptions:

- we assume that only single-scattering processes are relevant. This is a reasonable assumption given the largely open structure of the gas station. Note that the concept of "equivalent scatterer location" of [24] is not directly applicable in our model, because it is only defined for relatively small sizes of the virtual array.
- propagation occurs only in the horizontal plane. Due to our measurement setup (linear virtual array), identification of the elevation angle of the radiation, and thus height-coordinate of the scatterers, is not possible. Given the geometry of the setup, it is reasonable to assume that scattering could occur from the ground, as well as from the roof above the gas pumps. Since the echoes from the ground and roof do not propagate in the horizontal plane, the position the of scatterers extracted with the horizontal-only assumption will be off. Nevertheless, the arriving delays of these components are similar to the delays of MPCs that are reflected at the wall behind the BS antenna, and are therefore detected as part of the same cluster (see below).
- we assume that the temporal distortions by the scattering process can be neglected. It is well known [19] that in its most general case, the UWB impulse response can be modeled as

$$x(\tau) = \sum_{k=1}^{N} \alpha_k \chi_k(\tau) * \delta(\tau - \tau_k), \tag{1}$$

where $\chi_k(\tau)$ denotes the distortion of the k^{th} arriving component due to the frequency selectivity of the interactions with the environment, α_k its amplitude and τ_k the corresponding delay. N is the number of scatterers, and $*$ denotes the convolution operation. Nevertheless, since the distortion functions are in general not known, this model can not be applied to scatterer detection. By using the simplified model

$$x(\tau) = \sum_{k=1}^{L} \alpha_k \delta(\tau - \tau_k), \tag{2}$$

where $L > N$, a distorted pulse looks like a sequence of closely-spaced pulses with amplitudes determined by the power carried by the MPC as well as the pulse distortion. Thus, the simplified model might ultimately identify more scatterers than physically exist, thus generating so-called ghost components but their locations will be closely spaced around the locations of the true scatterers.

Despite the restrictions and caveats mentioned above, our scatterer location algorithm works well - this is confirmed by the fact that the extracted locations correspond well to the location of physical objects (gas pumps, columns, etc.) in our environments.

B. Scatterer Detection Method – Mathematical Formulation

A simplified flowchart of the method steps is given in Fig. 5. The method proceeds in an inner and an outer loop.

Step I: The inner loop runs for each array position, detecting iteratively with high-resolution the peaks in the impulse response with the highest amplitude. The loop stops when all peaks with an amplitude above a user-defined threshold are found.

Step II: Identification of the scatterer locations corresponding to the peaks detected in *Step I*. This is done by a spatial grid search where every grid point is a candidate scatterer (CS). Each CS is then associated with the peaks (of *all* impulse responses), from which we also deduce the visibility region and overall weight of the CS.

Step III: The CS with the strongest weight is chosen, and its contribution is subtracted from the original measured data. This defines the outer loop, which restarts from *Step I* with the updated data. The process continues until no more CSs are to be analyzed. The mathematical formulation of the above follows.

The measurement data is available in the frequency domain. The (complex) transfer function at the N_f frequency points are written into a vector $\mathbf{h}_i \in \mathbb{C}^{N_F \times 1}$,

$$\mathbf{h}_i = \left[\begin{array}{ccc} h_0 & \cdots & h_{N_F-1} \end{array} \right]^T. \tag{3}$$

where $(\cdot)^T$ is the transpose operator and i is indexing the different array positions. Since our channel model (2) is defined in the time domain, we can obtain a continuous channel impulse response $x(\tau)$ as

$$x(\tau) = \mathbf{p}^T(\tau)\mathbf{h}_i, \tag{4}$$

where $\mathbf{p}(\tau) \in \mathbb{C}^{N_F \times 1}$ is the vector of the IDFT (inverse discrete Fourier transform) coefficients, i.e.,

$$\mathbf{p}(\tau) = \left[\begin{array}{ccc} e^{j2\pi f_0 \tau} & \cdots & e^{j2\pi (f_0 + (N_F-1)\Delta f)\tau} \end{array} \right]^T,$$

where f_0 is the lowest measured frequency, and Δf is the frequency step.

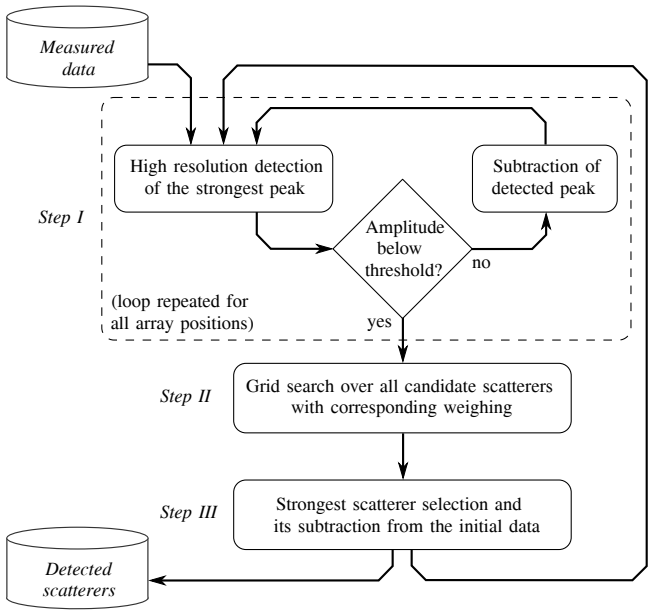

Fig. 5: Simplified flowchart of the scatterer detection method.

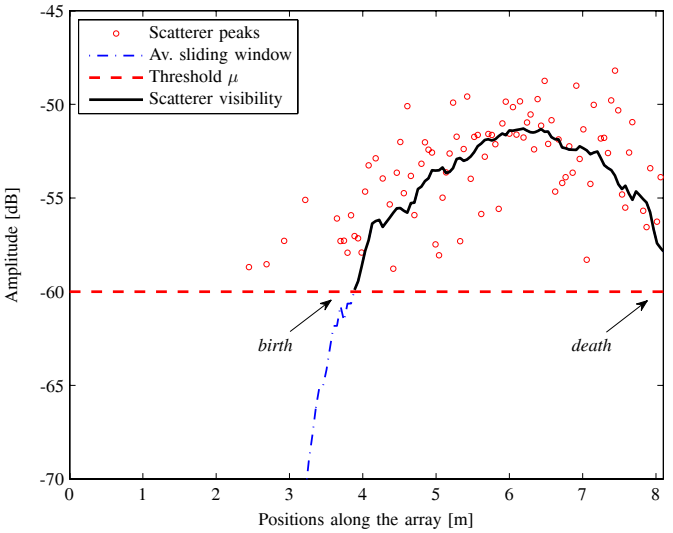

Fig. 6: Selected peak amplitudes and corresponding visibility region for an example scatterer. The array positions without a selected peak, are considered to have zero amplitude on the ASW calculation.

The peak search step can be formulated as the maximization of the impulse response envelope over the delay variable τ. Since τ is a continuous variable which can take any real value, our resolution can be arbitrarily high. The estimated delay of the i:th array position and l:th strongest peak then becomes

$$\hat{\tau}_{i,l} = \arg\max_{\tau} \left| \mathbf{p}^T(\tau)\mathbf{h}_{i,l} \right|, \tag{5}$$

and the corresponding complex amplitude is obtained as

$$\hat{\alpha}_{i,l} = \frac{\mathbf{p}^T(\hat{\tau}_{i,l})\mathbf{h}_{i,l}}{\mathbf{p}^T\mathbf{p}}. \tag{6}$$

The vector $\mathbf{h}_{i,l}$ is defined as the impulse response remaining after the contribution of the $l-1$ th peak has been subtracted, i.e.,

$$\mathbf{h}_{i,l} = \begin{cases} \mathbf{h}_i, & l = 1 \\ \mathbf{h}_{i,l-1} - \hat{\alpha}_{i,l-1}\mathbf{p}^*(\hat{\tau}_{i,l-1}), & l > 1 \end{cases} \tag{7}$$

where $(\cdot)^*$ denotes complex conjugation. Note that the subtraction is performed not in the *transform* domain (i.e., delay domain), but over the same domain that the data were measured, i.e., the frequency domain. The process continues until the estimated peak amplitude $|\hat{\alpha}_{i,l}|$ falls below a predefined threshold μ.[2] For our data, we chose to set this threshold corresponding to a signal power of -99 dB which was 20 dB above the estimated noise floor at -119 dB. At a distance of 11.17 m between the antennas, this threshold was still 25 dB below the LOS power, as illustrated in Fig. 7. The peak detection process is repeated for all the array positions.

The next step consists of finding the point scatterers in the two-dimensional *geometrical* space that match with the detected peaks in the impulse response. To find those scatterers we scan for their presence over all the array positions simultaneously. This is accomplished by a grid search where every geographical point is a candidate scatterer (CS). The step of the grid search was 10 mm, which is four times smaller than the spacing of the virtual array positions. In order to find the strongest CS, we determine their respective *weights* as described subsequently.

For each CS, we calculate the theoretical propagation delay for all the MS positions, assuming a single bounce on the CS and wave propagation at the speed of light. Then, a peak of the impulse response is associated with a CS if its propagation delay agrees with the CS's theoretical delay within the delay resolution of our system (the inverse of the bandwidth). From this rule, a given CS can have at most N_{MS} peaks associated to it, one for each array position.

Since our measurements covered large distances, certain scatterers might not be "visible" over the whole array, i.e., do not have peaks of the impulse response associated with them for all positions of the MS along the rail. We therefore define the *visibility region* of a scatterer. To this end, we use an average sliding window (ASW) over the associated peak amplitudes, which for the k^{th} CS is

$$\mathbf{w}_k[i] = \frac{1}{N_W} \sum_{n=-N_W/2}^{N_W/2-1} \alpha_{n+i,k}.$$

Here, N_W is the window size and α are the peak amplitudes. The window slides over the consecutive array positions as $i = 1, \ldots, N_i$. We used a window size corresponding to an area of one meter, the size of the expected region of stationarity.[3] The locations where the ASW crosses the threshold μ define the *birth* and *death* of the CS, and the visibility region is defined as the region between birth and death location. Finally, the *weight* of a CS is defined as the integrated power of the impulse response peaks associated with a CS that lie within its visibility region. An illustrative example of the visibility region of a scatterer, and corresponding birth and death positions, can be seen in Fig. 6.

[2] An illustrative example of the peak search step, and corresponding detected peaks, can be found in [1] Fig. 2.

[3] The justification for the choice of one meter stems from the fact that all significant scatterers are visible for at least one meter along the array (cf. Fig. 4).

After weighting, it is possible to select the strongest CS and save its information in a data base. Using again the successive cancellation principle, the measured frequency responses are updated by subtracting the contributions to the impulse responses by this scatterer before the detection of the next. The update is defined as

$$\mathbf{h}_i = \mathbf{h}_i - \hat{\alpha}_{i,l_{\text{peak}}} \mathbf{p}^* \left(\hat{\tau}_{i,l_{\text{peak}}} \right) \tag{8}$$

for all the array positions whose impulse responses have a peak associated with the scatterer, where $\alpha_{i,l_{\text{peak}}}$ and $\hat{\tau}_{i,l_{\text{peak}}}$ are the estimated delay and complex amplitude corresponding to the MPC of the selected scatterer at the array position i. At this point, the process is repeated starting from the high resolution peak search.

The output of the method above also provides us with the information on how the contribution from a given scatterer evolves along the array (for different MS positions). This means that we can track the MPCs associated with the scatterers. An example of tracking is shown in Figs. 7(a) and 7(b). In Fig. 7(a), eight detected scatterers are identified with a marker and labeled with a letter, $\{a, \ldots, h\}$. To ease the visual interpretation, MPCs with similar delays are also given similar markers. MPCs a and b, are the LOS and back wall reflection, respectively, and the remaining MPCs originate from different metal objects. Fig. 7(b) shows the MPC delays corresponding of the same scatterers after moving the antenna 1.34 m away from the initial location.

By comparing both figures, it can be seen how some scatterers maintain their relative delays while the delays between some other components changes. The four MPCs with circle markers, for example, initially have similar delays, and it might be conjectured that their corresponding scatterers are in similar spatial locations. However, with the movement of the antenna, they evolve separately in two sub-groups, $\{e, g\}$ and $\{f, h\}$, revealing that those two groups of scatterers do not originate from the same physical location. By matching the detected scatterers with the real environment, it was found that $\{e, g\}$ belonged to a publicity sign and $\{f, h\}$ to a gas pump which were actually separated by 13 m.

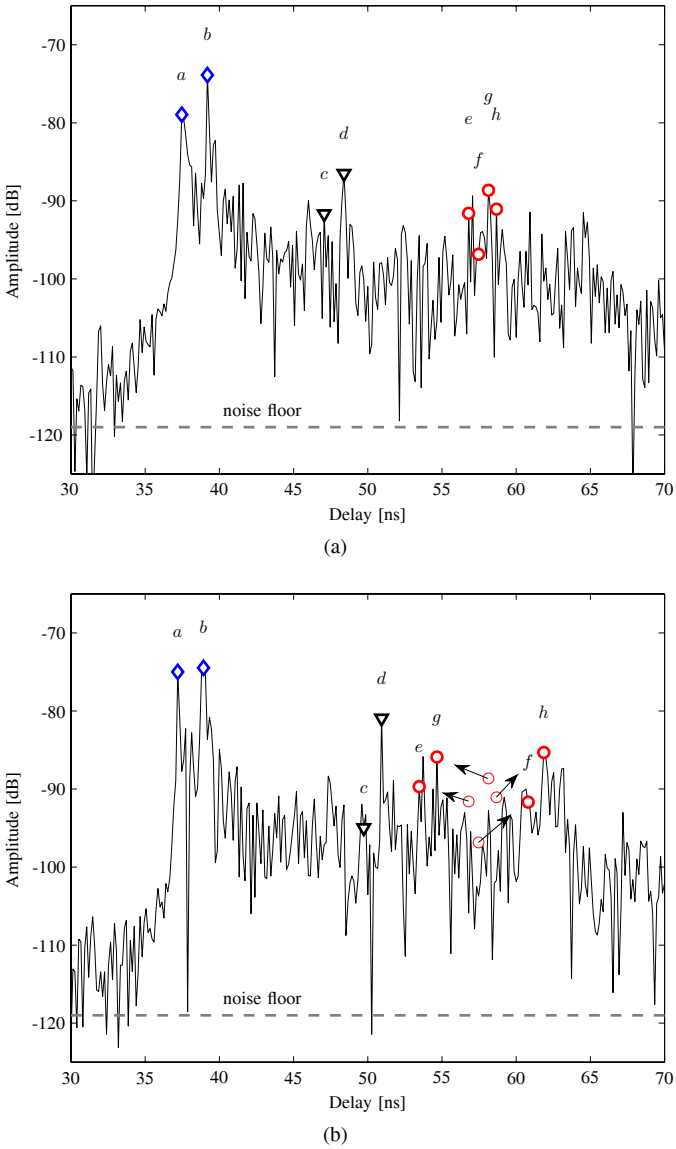

Fig. 7: Scatterer tracking example from the UWB impulse response where the labeled components were found using the method described in Section III-B: (a) at position $(x = -1.57, y = 11.06)$ and (b) at position $(x = -0.23, y = 11.06)$.

C. Clustering the Detected Scatterers Using a Modified K-means Approach

It is well established in the literature that scatterer locations tend to be *clustered*. (see, e.g., [25]–[27]). Here we define a *cluster as a group of scatterers located a similar points in space*. Clustering can give additional physical insights into the propagation mechanisms, and is also useful in the establishment of simple yet accurate channel models. Both visual inspection [26] and automated clustering [27] have been proposed in the literature; we use the latter approach in this paper.

The *K*-means clustering algorithm [28] groups the scatterers by minimizing the Euclidean distance from the scatterers to the cluster centroids, over all clusters. The distance metric used here was modified to minimize the power-weighted geometrical distances.[4] In other words, we scale the geometric distance to the centroid by the scatterer power, such that the distance metric from a scatterer at position (x_s, y_s) with power P_s to a centroid at (x_c, y_c) is given by

$$d_{\text{metric}} = P_s \sqrt{(x_s - x_c)^2 + (y_s - y_c)^2}. \tag{9}$$

With this approach, the position of the centroids will be more dependent of the position of a stronger scatterer than of a weaker one. The definition is similar to the "center of gravity", and follows from the intuitive idea that for a specific cluster positions, it is more likely to find stronger components around its center, and also solves the problem of weaker, far-away scatterers pulling the centroid excessively away from the true

[4]Since our data is defined in three dimensions (*x-coord*, *y-coord*, *power*), a straightforward application is to perform the clustering equally over all the dimensions. This is not reasonable, since it results in the grouping of scatterers also by their level of power, which doesn't agree with the observed measurements.

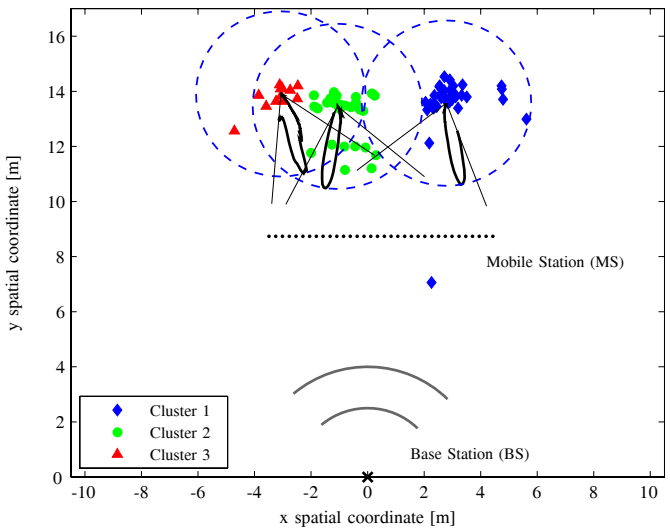

Fig. 8: Estimated radiation pattern of three clusters of scatterers. The cluster at the base station is not shown.

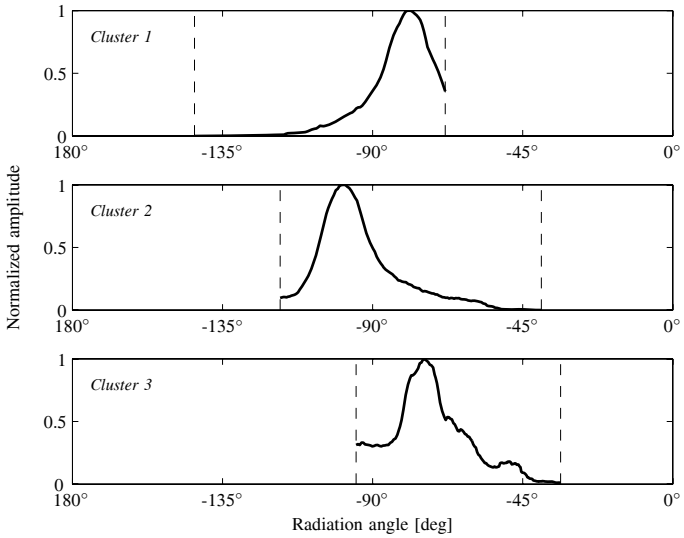

Fig. 9: Estimated radiation pattern of three channel clusters in the angular domain.

center. This definition was first proposed in [27] and referred to as the KPowerMeans algorithm.

The *K*-means algorithm is iterative, and thus requires an initial estimate of the cluster position. Since from our measurement campaigns, we had a good knowledge of the environment surrounding the antennas, we made use of it to select the initial parameters. The positions in space matching physical objects and scatterers were set as initial cluster positions. This was found to be preferable to blind methods, since it reduces clustering errors.[5]

An example of the output of the clustering algorithm is illustrated in Fig. 8, where different clusters were given different markers and colors.

IV. Cluster Directional Properties and Shadowing

A. Cluster Directional Properties

The power of the MPC associated with a specific scatterer, as well as the sum of the powers of the MPCs associated with a cluster, varied over the different MS positions. To better interpret these variations, we investigate in this subsection whether the power variations of a given MPC are correlated with the power variations of the other MPCs associated with the same cluster of scatterers. Furthermore, we show that these variations can be compactly described in the angular domain.

As examples, we choose three sets of clustered scatterers depicted in Fig. 8. Since the propagation paths between a given scatterer and different MS positions have different path loss due to the different runlengths the signal has to cover, we compensate these losses using a d^{-n} distance power law. The pathloss coefficient $n = 1.38$ was obtained from a least-squares fit using all available data, see [18] subsection II-D. The resulting normalized receive power as a function of the angle under which the MS "sees" the scatterer is henceforth called the "radiation pattern" of the scatterer. The covered angular range in the azimuth plane is limited, but is similar for the scatterers belonging to the same cluster. Given that our interest is on the directional properties of the scatterers, and not on their relative level of power, each radiation pattern is normalized such that the maximum has unit amplitude.

Subsequently, the radiation pattern of the scatterers within a cluster were averaged to form the cluster radiation pattern. The resulting patterns are also shown in Fig. 8, centered on the corresponding clusters. From the figure, one can observe that each cluster radiates in a preferred direction with a beam-like shape. Fig. 9 shows the same radiation patterns, but plotted directly in the angular domain. It can be seen that the radiation patterns are approximately symmetrical with respect to the angle of maximum radiation.

The results presented here are from a single virtual array, but these directional characteristics of the group of scatterers were found throughout all our measurements. The patterns vary in width and shape from cluster to cluster, but a preferred direction of radiation is always identifiable. It is important to stress here that these amplitude variations are not originated by shadowing from obstructing objects but by the characteristics of the physical objects themselves.

B. Shadowing Behind Objects

In some of our measurements, there were MS positions for which no LOS existed between TX and RX. This occurred when the MS antenna was in the shadow region of a physical object, such as a gas pump or a column. In this section, we investigate the behavior of the received signal while the MS was being moved through such shadow regions.

When the MS is entering a shadow region of a given object, the signal strength starts to decay from its LOS value. The inverse process takes place when the MS is leaving the shadow region. Furthermore, on several occasions, a well defined amplitude peak is observed when the MS is exactly behind the shadowing object, in the center of the shadow region. This peak can be explained qualitatively by diffraction theory. Since there are two main diffraction components, one from

[5]A clustering error occurs when a calculated centroid ends up where no physical object exists – a situation often related to the algorithm converging to a local minimum.

each side of the shadowing object, these two components can add constructively behind the object, to create a *peak*.

For the description of the diffraction field in UWB communications, several useful results are available in the literature: e.g., the recent work by Zhou and Qiu [29], provides closed-form expressions for the impulse responses of several canonical channels. Other fundamental work in this topic pertaining to the time domain is [30]–[32]. Here, we use the well known frequency domain[6] expressions of the uniform geometrical theory of diffraction (UTD/GTD) [33], i.e.,

$$E_d(s) = E_i D(\hat{s}, \hat{s}') A_d(s) e^{-jks}, \tag{10}$$

in which s is the distance between the diffraction edge and the observation point, E_i is the incident field on the edge, $D(\hat{s}, \hat{s}')$ is the dyadic diffraction coefficient, $A_d(s)$ describes how the amplitude of the field varies along the diffracted ray and k is the wave number.[7]

Fig. 10 compares the first received component from the MS behind a steel pillar, extracted from the measurements, with the predicted electrical field behind a perfectly electric conductor (PEC) plate in the same location. The PEC plate was chosen for the comparison because it is the geometry that among all canonical geometries is the closest to the steel pillar, it leads to straight wedge diffraction. For the simulation, the diffracted field was assumed to be constituted by two components, one for each side of the plate; both calculated from (10). Since the cross section of the pillar was 0.3×0.3 m, the simulated object (also 0.3 m wide) was at least three times larger than any of the considered wavelengths, which supports the validity of (10).

The measured signal was normalized to the strength of the hypothetical LOS signal (i.e., in the absence of shadowing objects). Since there was no perfect knowledge of the transmitted pulse shape, a frequency flat pulse was used in the simulation. The figure shows a qualitative match, but no perfect quantitative agreement. This is to be expected, because the shape and electromagnetic properties of the actual pillar did not agree with the "two-wedge" model used in the theoretical computations.

V. Conclusions

In this work, we have described the results from one of the few existing UWB outdoor measurement campaigns. The target scenario was a gas station, an environment envisioned in the context of UWB-based infostations. We have described a scatterer detection method which is suitable for UWB outdoor measurements deploying a virtual array covering long distances.

The tracking capabilities of the method showed how the delays of MPCs change within the impulse response as the MS moves. The analysis of the cluster directional properties showed that groups of scatterers have a preferred direction of radiation and often the shape of their radiation pattern approaches the one of a directional beam. This knowledge is of valuable help for the development of more accurate, non-purely statistical, channel models. The study of the shadow effects on the UWB signal envelope revealed an increase of the signal amplitude was often found when one of the antennas was exactly behind a shadowing object; diffraction theory was shown to give a good explanation to this effect.

[6]The frequency domain expressions were used instead of the time domain ones, since the measurements were also performed in the frequency domain.

[7]A complete definition of $E_d(s)$ and all of its components is given in detail in [33].

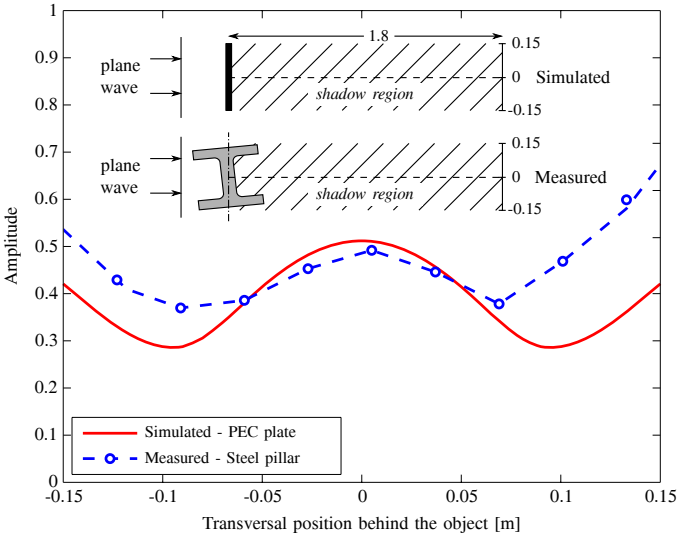

Fig. 10: Simulated and measured signal amplitudes behind shadow objects. The upper sketches illustrate the simulated and measured geometries. The incident wave is considered plane since in the measured scenario the BS antenna was 14 m away from the pillar.

VI. Acknowledgments

The authors would like to thank Dr. R. Qiu for the helpful discussion regarding the diffraction issues. We also thank the reviewers of this manuscript for their constructive remarks.

References

[1] T. Santos, J. Karedal, P. Almers, F. Tufvesson, and A. F. Molisch, "Scatterer detection by successive cancellation for UWB–method and experimental verification," in *Proc. IEEE Veh. Technol. Conf. (VTC'08–Spring)*, May 2008, pp. 445–449.

[2] M.-G. Di Benedetto, T. Kaiser, A. F. Molisch, I. Oppermann, C. Politano, and D. Porcino (eds.), *UWB Communications Systems: A Comprehensive Overview*. EURASIP publishing, 2005.

[3] X. Shen, M. Guizani, R. C. Qiu, and T. Le-Ngoc, *Ultra Wideband Wireless Communications and Networks*. John Wiley, 2006.

[4] Z. Sahinoglu and S. Gezici, "Ranging in the IEEE 802.15.4a standard," in *Proc. IEEE Annual Wireless and Microwave Technol. Conf.*, pp. 1–5, 2006.

[5] R. A. Scholtz, D. M. Pozar, and W. Namgoong, "Ultra-wideband radio," *J. Applied Signal Process.*, no. 3, pp. 252–272, 2005.

[6] M. Win and R. Scholtz, "On the energy capture of ultrawide bandwidth signals in dense multipath environments," *IEEE Commun. Lett.*, vol. 2, no. 9, pp. 245–247, Sep. 1998.

[7] A. Batra, J. Balakrishnan, and A. Dabak, "Multi-band OFDM: a new approach for UWB," in *Proc. Int. Symp. on Circuits and Systems*, 2004, pp. 365–368.

[8] "High rate ultra wideband PHY and MAC standard ECMA-368, 3rd edition," Dec. 2008.

[9] R. Frenkiel, B. Badrinath, J. Borres, and R. Yates, "The infostations challenge: balancing cost and ubiquity in delivering wireless data," *IEEE Personal Commun.*, vol. 7, no. 2, pp. 66–71, 2000.

[10] DaimlerChrysler, "DaimlerChrysler to demonstrate first of its kind invehicle video streaming over UWB at CES WiMedia techzone," Jan. 2007.

[11] M. Z. Win, F. Ramirez-Mireles, R. A. Scholtz, and M. A. Barnes, "Ultra-wide bandwidth (UWB) signal propagation for outdoor wireless communications," in *Proc. IEEE Veh. Technol. Conf. (VTC'97–Spring)*, 1997, pp. 251–255.
[12] "UWB channel measurements and modeling for DARPA NETEX," Virginia Tech, 2004.
[13] M. D. Renzo, F. Graziosi, R. Minutolo, M. Montanari, and F. Santucci, "The ultra-wide bandwidth outdoor channel: from measurement campaign to statistical modelling," *Mobile Networks and Applications*, vol. 11, no. 4, pp. 451–467, 2006.
[14] C. Kim, X. Sun, L. Chiam, B. Kannan, F. Chin, and H. Garg, "Characterization of ultra-wideband channels for outdoor office environment," in *Proc. IEEE Wireless Commun. Networking Conf.*, vol. 2, 2005, pp. 950–955.
[15] S. Emami, C. Corral, and G. Rasor, "Ultra-wideband outdoor channel modeling using ray tracing techniques," in *Proc. IEEE Consumer Commun. Networking Conf.*, Jan. 2005, pp. 466–470.
[16] A. F. Molisch, D. Cassioli, C.-C. Chong, S. Emami, A. Fort, B. Kannan, J. Karedal, J. Kunisch, H. G. Schantz, K. Siwiak, and M. Z. Win, "A comprehensive standardized model for ultrawideband propagation channels," *IEEE Trans. Antennas Propag.*, vol. 54, no. 11, pp. 3151–3166, Nov. 2006.
[17] A. Domazetovic, L. J. Greenstein, N. B. Mandayam, and I. Seskar, "A new modeling approach for wireless channels with predictable path geometries," in *Proc. IEEE Veh. Technol. Conf. (VTC'02–Fall)*, vol. 1, Sep. 2002, pp. 454–458.
[18] T. Santos, F. Tufvesson, and A. F. Molisch, "Modeling the ultra-wideband outdoor channel–model specification and validation," 2009, submitted to *IEEE Trans. Wireless Commun.*
[19] A. F. Molisch, "Ultrawideband propagation channels-theory, measurement, and modeling," *IEEE Trans. Veh. Technol.*, vol. 54, no. 5, pp. 1528–1545, Sep. 2005.
[20] F. Harrysson, J. Medbo, A. F. Molisch, A. Johansson, and F. Tufvesson, "The composite channel method: efficient experimental evaluation of a realistic MIMO terminal in the presence of a human body," in *Proc. IEEE Veh. Technol. Conf. (VTC'08–Spring)*, May 2008, pp. 473–477.
[21] F. Berens, H. Dunger, S. Czarnecki, T. Bock, R. Reuter, S. Zeisberg, J. Weber, and J. Guasch, "UWB car attenuation measurements," in *Proc. IST Mobile and Wireless Communications Summit*, 2007, pp. 1–5.
[22] R.-M. Cramer, R. Scholtz, and M. Win, "Evaluation of an ultra-wideband propagation channel," *IEEE Trans. Antennas Propag.*, vol. 50, no. 5, pp. 561–570, 2002.
[23] K. Haneda and J.-I. Takada, "An application of SAGE algorithm for UWB propagation channel estimation," in *Proc. IEEE Conf. Ultra Wideband Syst. Technol. Digest Techn. Papers*, 2003, pp. 483–487.
[24] A. F. Molisch, A. Kuchar, J. Laurila, K. Hugl, and R. Schmalenberger, "Geometry-based directional model for mobile radio channels-principles and implementation," in *Proc. European Trans. on Telecommunications*, vol. 14, no. 4, 2003, pp. 351–359.
[25] A. F. Molisch, H. Asplund, R. Heddergott, M. Steinbauer, and T. Zwick, "The COST259 directional channel model part I: overview and methodology," *IEEE Trans. Veh. Commun.*, vol. 5, no. 12, pp. 3421–3433, Dec. 2006.
[26] M. Toeltsch, J. Laurila, K. Kalliola, A. Molisch, P. Vainikainen, and E. Bonek, "Statistical characterization of urban spatial radio channels," *IEEE J. Sel. Areas Commun.*, vol. 20, no. 3, pp. 539–549, 2002.
[27] N. Czink, P. Cera, J. Salo, E. Bonek, J.-P. Nuutinen, and J. Ylitalo, "A framework for automatic clustering of parametric MIMO channel data including path powers," in *Proc. IEEE Veh. Technol. Conf. (VTC'06–Fall)*, Sep. 2006, pp. 1–5.
[28] J. A. Hartigan and M. A. Wong, "Algorithm AS 136: a K-means clustering algorithm," *Applied Statistics*, vol. 28, no. 1, pp. 100–108, 1979.
[29] C. Zhou and R. C. Qiu, "Pulse distortion and optimum transmit waveform for pulse-based UWB communications," *Int. J. Ultra Wideband Commun. and Systems*, vol. 1, pp. 32–48, 2009.
[30] T. W. Veruttipong, "Time domain version of the uniform GTD," *IEEE Trans. Antennas Propag.*, vol. 38, no. 11, pp. 1757–1764, Nov. 1990.
[31] P. R. Rousseau and P. H. Pathak, "Time-domain uniform geometrical theory of diffraction for a curved wedge," *IEEE Trans. Antennas Propag.*, vol. 43, no. 12, pp. 1375–1382, Dec. 1995.
[32] P. R. Rousseau, P. H. Pathak, and H.-T. Chou, "A time domain formulation of the uniform geometrical theory of diffraction for scattering from a smooth convex surface," *IEEE Trans. Antennas Propag.*, vol. 55, no. 6, pp. 1522–1534, June 2007.
[33] R. Kouyoumjian and P. Pathak, "A uniform geometrical theory of diffraction for an edge in a perfectly conducting surface," *Proc. IEEE*, vol. 62, no. 11, pp. 1448–1461, Nov. 1974.

Telmo Santos received his M.S. degree in electronics and computer engineering in 2005 from Coimbra University, Portugal, and his Licentiate degree in wireless communications in 2009, from Lund University, Sweden. He is currently a Ph.D. student at the Department of Electrical and Information Technology, Lund University, where his main research interests concern measurements and modeling of wireless propagation channels for UWB systems and antenna selection schemes for MIMO systems.

Johan Karedal received his M.S. degree in engineering physics in 2002 and his Ph.D. in radio communications in 2009, both from Lund University, Sweden. He is currently a postdoctoral fellow at the Department of Electrical and Information Technology, Lund University, where his main research interests concern measurements and modeling of wireless propagation channels for MIMO and UWB systems. Dr. Karedal has participated in the European research initiative "MAGNET."

Peter Almers received a M.S. degree in electrical engineering and a Ph.D. degree in radio systems from Lund University, Lund, Sweden, in 1998 and 2007, respectively. Since late 2008 he joined ST-Ericsson in Lund. Dr. Almers received the IEEE Best Student Paper Award at the 2002 International Symposium on Personal, Indoor, and Mobile Radio Communications.

Fredrik Tufvesson was born in Lund, Sweden in 1970. He received the M.S. degree in electrical engineering in 1994, the Licentiate Degree in 1998 and his Ph.D. in 2000, all from Lund University in Sweden. After almost two years at a startup company, Fiberless Society, Fredrik is now associate professor at the Department of Electrical and Information Technology. His main research interests are channel measurements and modeling for wireless MIMO and UWB systems. Beside this, he also works with radio based search and rescue systems.

Andreas F. Molisch is Professor of Electrical Engineering at the University of Southern California, Los Angeles, CA, USA. His current research interests are measurement and modeling of mobile radio channels, UWB, cooperative communications, and MIMO systems. He has authored, co-authored or edited four books, eleven book chapters, more than 120 journal papers, and numerous conference contributions, as well as more than 70 patents and 60 standards contributions. He has been an editor of a number of journals and special issues, General Chair, TPC Chair, or Symposium Chair of multiple international conferences, and chairman of various international standardization groups. He is a Fellow of the IEEE, a Fellow of the IET, an IEEE Distinguished Lecturer, and recipient of several awards.